Biomaterials Science

PAPER

View Article Online
View Journal | View Issue

Cite this: *Biomater. Sci.*, 2018, **6**, 2448

Osseointegration of ultrafine-grained titanium with a hydrophilic nano-patterned surface: an *in vivo* examination in miniature pigs

Vivianne Chappuis, *[a] Laura Maestre,[a] Alexander Bürki,[b] Sébastien Barré,[c] Daniel Buser,[a] Philippe Zysset [b] and Dieter Bosshardt[d]

Advances in biomaterials science and implant surface technology have made dental implants more predictable and implant therapy more attractive to patients. Surgical interventions are becoming less invasive, and patients heal faster and suffer less morbidity. In this preclinical *in vivo* study, we compared a new ultra-fine grained titanium (ufgTi) implant material with a hydrophilic nano-patterned surface to commercially pure titanium (cpTi) in a well-established animal model. CpTi grade 4 was subjected to Equal Channel Angular Pressing (ECAP), followed by a cold drawing process that provided ultra-fine-grained titanium (ufgTi) with a mean grain size of 300 nm. After metallographic assessment, the surface topography was characterized by laser confocal microscopy and atomic force microscopy. UfgTi and cpTi implants were inserted in the mandible and maxilla of miniature pigs that healed for 4 and for 8 weeks. Osseointegration was assessed by biomechanical torque out analysis, histomorphometric evaluation, and micro-CT analysis. The metallographic properties of UfgTi were significantly better than those of cpTi. Their surface topographies had similar hydrophilic nano-patterned characteristics, with no significant differences in the nanometre range. Histomorphometric and biomechanical torque out analysis revealed no significant differences between ufgTi and cpTi in environments of either low (maxilla) or high (mandible) bone density. We obtained high bone-to-implant contact values irrespective of the bony microarchitecture even when the bone mineral density was low. Overall, this investigation suggests that ufgTi forms a hydrophilic nano-patterned surface with superior metallographic properties compared to cpTi and high levels of osseointegration. Thus, ufgTi has therapeutic potential as a future strategy for the development of small diameter implants to enable less invasive treatment concepts, reduce patient morbidity and may also lower the costs of patient care.

Received 17th June 2018,
Accepted 3rd July 2018

DOI: 10.1039/c8bm00671g

rsc.li/biomaterials-science

1. Introduction

Osseointegration has developed into a key discipline in dental medicine for rehabilitating fully and partially edentulous patients.[1] Two research groups pioneered this concept in studies that prototyped commercially pure titanium (cpTi) implants.[2–5] Mid- to long-term studies demonstrated their satisfactory outcomes.[6–10] Today, improving the predictability and the attractiveness of implant therapy for patients has become a priority. New surface developments critically improve cell proliferation and differentiation, significantly enhancing osseointegration and reducing the healing time.[11–14] Research has also focused on making dental implants stronger and thereby smaller. Small-diameter implants reduce the need to regenerate tissues in simultaneous or staged procedures, diminish the invasiveness and morbidity of surgical interventions and therefore may also lower the cost of treatment. New dental implant biomaterials that support less invasive therapies must withstand strong masticatory forces and maintain osseointegration for the increasing lifespan of patients.[15] Titanium alloys offer an advantage over cpTi because they are stronger and thus more resistant to fatigue,[16] but some alloys contain potentially toxic alloying elements.[17,18] It is possible that strengthening titanium by refining the grains to enhance its mechanical

[a]*Department of Oral Surgery and Stomatology, School of Dental Medicine, University of Bern, Freiburgstrasse 7, 3010 Bern, Switzerland. E-mail: vivianne.chappuis@zmk.unibe.ch, lauramaestre@hotmail.com, daniel.buser@zmk.unibe.ch; Fax: +4131632 25 03; Tel: +4131 632 25 45*
[b]*Institute for Surgical Technology and Biomechanics, University of Bern, Stauffacherstrasse 78, 3014 Bern, Switzerland. E-mail: alexander.buerki@gmx.ch, philippe.zysset@istb.unibe.ch*
[c]*Topographic and Clinical Anatomy, University of Bern, Baltzerstrasse 2, 3000 Bern 9, Switzerland. E-mail: sebastien.f.barre@gmail.com*
[d]*Robert K. Schenk Laboratory of Oral Histology, School of Dental Medicine, University of Bern, Freiburgstrasse 7, 3010 Bern, Switzerland. E-mail: dieter.bosshardt@zmk.unibe.ch*

properties may prove to be a valuable alternative to titanium alloys.[19] Reinforcement of titanium by grain refinement could open the door to less invasive therapies.

Titanium can be reinforced by grain refinement that uses Equal Channel Angular Pressing (ECAP).[20] Refining the grains strengthens cpTi because it forms a submicron or nanoscale grain structure. Grain size, a significant micro-structural factor, influences nearly all aspects of the physical and mechanical behaviours of polycrystalline metals and their chemical and biochemical responses to the surrounding tissue.[21] ECAP may refine the grain size of cpTi to <1 μm.[22,23] When ECAP is used to reduce the average grain size from 30 μm to 150 nm for grade 4 titanium by forging and drawing, the material's tensile strength increases from 700 to 1420 MPa.[24] *In vitro*, such ultrafine-grained titanium (ufgTi) surfaces enhance stem cell adhesion and spreading in the initial phase after seeding[25,26] and also limit the ability of some strains of bacteria to adhere to ufgTi surfaces.[27] Therefore, refining the micro-structural grains of ufgTi may also target specific eukaryotic and prokaryotic cell responses.[28,29] Obtaining enhanced metallographic properties by ECAP combined with these surface characteristics targeting specific cell responses may represent a future strategy for small-diameter implants to facilitate less invasive treatment concepts.

The surface topography can promote osseointegration and reduce the healing time. Surface technologies that use sandblasting and acid-etching to change the topography and chemistry from a rather smooth machined surface to a more micro-rough surface also increase the speed of osseointegration, evidenced by more bone-to-implant contact (BIC) and higher removal torque values (RTV).[12,30,31] These micro-rough surfaces are now the standard of care in dental implant applications and have excellent long-term outcomes.[32,33] On the micrometre scale, we can see that ufgTi has a similar hydrophilic micro-rough surface characteristic, but we still know little about the differences at the nanometre level and their related effects on osseointegration. Nano-patterned surfaces modulate cell adhesion through direct cell-to-surface interactions and indirectly by promoting protein-to-surface interconnection mechanisms.[34] These initial protein-to-surface interactions may control osteoblast adhesion that is often mediated through integrins.[35,36] Surface energy or hydrophilicity can further modify these interactions.[37,38] It may be possible to use hydrophilic nano-patterned surfaces to change protein interactions and control tissue formation at implant surfaces.[39] Since these nanotechnological devices are rapidly covered by selected groups of molecules that interact with the biological system, we must critically assess their biological impact before implementing them in a clinical setting.[40,41]

Since pre-clinical *in vivo* evaluation is essential for clinical applications, we set out to (i) characterize the metallographic properties and the surface topography of ufgTi implants *in vitro* through contact angle measurements, laser confocal microscopy, and atomic force microscopy, (ii) assess osseointegration of a hydrophilic nano-patterned implant surface *in vivo* in a well-established model in miniature pigs through histomorphometric and biomechanical torque out analysis, and (iii) measure the influence of the bony microarchitecture using micro-CT imaging.

2. Materials and methods

2.1. Preparation of titanium samples and implant design

cpTi grade 4 was subjected to equal channel angular pressing (ECAP) by route B_c (four times 90° rotation of the bar around the longitudinal axis after each pass) followed by a cold drawing process that produces an ultra-fine grained microstructure (Patent No.: US8919168)[42] received from Straumann AG, Basel, Switzerland. This well-documented grain refinement process ensured uniform grain fragmentation down to the submicrometre range. Carpenter Technology Inc. (Philadelphia, Pennsylvania, USA) supplied the material. The mean grain size was 300 nm. A metallographic assessment analysed ultimate tensile strength, yield strength, elongation, reduction area, elastic modulus and Vickers hardness.

The surfaces of both implants were treated alike: first they were sandblasted and then etched with an acid (SLActive, Straumann AG, Basel, Switzerland). As described above, two standardized implant designs were applied in the *in vivo* tests and subjected to biomechanical and histological evaluation:[12,43–45]

(a) *Biomechanical evaluation*: Removal torque out testing implants (RT) were 4.8 mm in diameter and 6 mm long (Straumann AG, Basel, Switzerland). An internal hexagonal connection was used for torque out evaluation[43–45] (Fig. 1A).

(b) *Histological evaluation*: Bone chamber implants (BC) were 4.2 mm in diameter and 6 mm long (Straumann AG, Basel, Switzerland). They revealed bone ingrowth into the chamber (Bone Density, BD) and bone-to-implant contact (BIC) at the implant surface.[12,45] The two circumferential chambers were 0.75 mm deep and 1.8 mm high (Fig. 1B).

2.2. Surface characterization

2.2.1. Contact angle measurements. Water-contact-angle measurements, using a sessile-drop test with ultrapure water (EasyDrop DSA20E, Krüss GmbH, Hamburg, Germany), assessed the wettability. Before being measured, the samples were blow-dried in a stream of argon. The droplet size for the contact-angle measurements was 0.1 μl; contact angles were calculated by fitting a circular segment function to the contour of the droplet placed on the surface.[46]

2.2.2. Electron microscopy. A field-emission-gun scanning electron microscope (SEM) was used to qualitatively evaluate the surface topography. High-resolution SEM images were captured with a Zeiss Supra 55 SEM (Carl Zeiss AG, Oberkochen, Germany) equipped with a field-emission electron source and an Everhart–Thornley secondary electron detector. The SEM images were acquired at an acceleration voltage of 15–20 kV. Ten ufgTi and 10 cpTi samples were analysed. Measurements were made at the Microscopy Centre of the University of Basel, Switzerland.

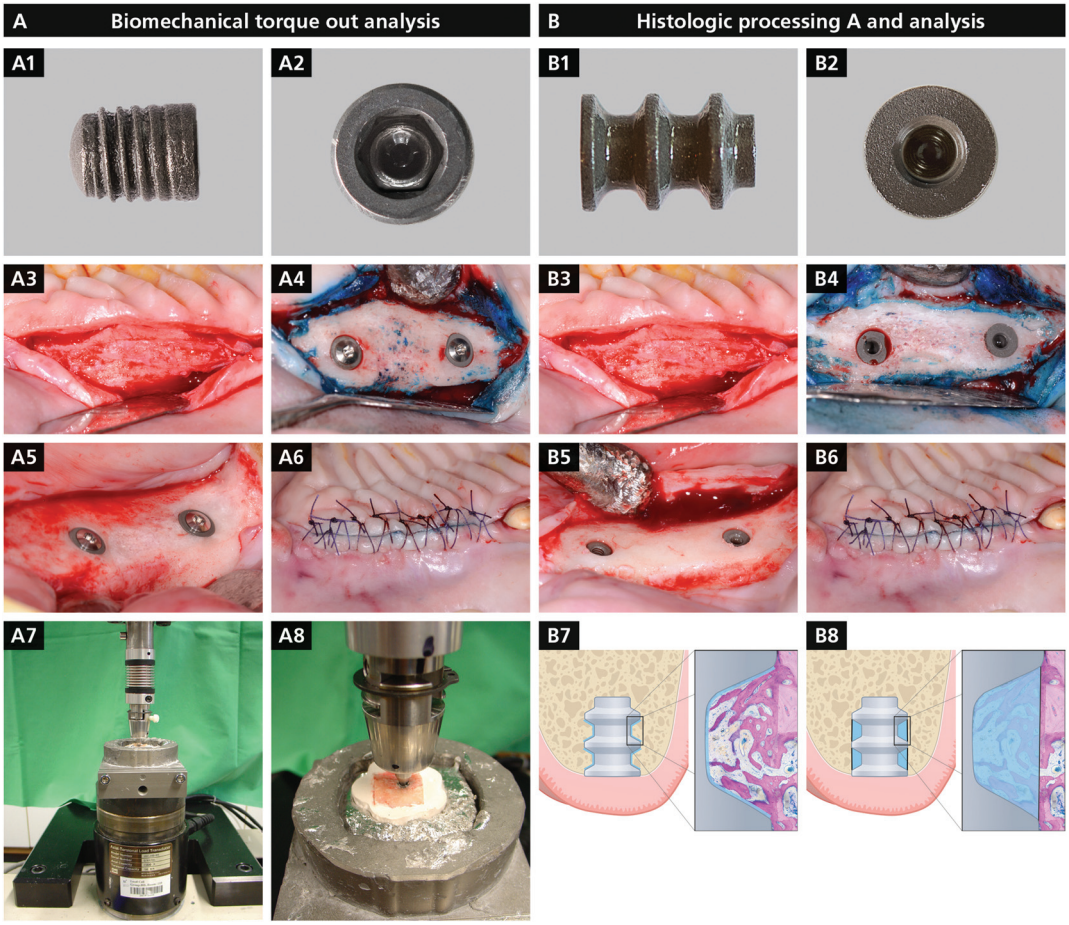

Fig. 1 Experimental design of the *in vivo* testing using biomechanical (A) and histological (B) analyses. (A1 and A2) Implant design: removal torque out testing implants (RT) were 4.8 mm in diameter and 6 mm long, with an internal hexagonal connection for torque out evaluation. (A3–6) Surgical procedure: one test (ufgTi) and one control (cpTi) were inserted on one side of the maxilla (A4) and the mandible (A5). The wound was primarily closed. (A7 and A8) Biomechanical analysis: the specimens were embedded in dental plaster and connected to the load cell. A low-melting point alloy was poured into the mould to create a rigid interface to the plaster. This procedure ensures axial alignment of the machine and the implant. The removal torque was tested by rotating the implant counter clockwise at 0.5° s^{-1} until the peak moment was clearly reached. (B1 and B2) Implant design: bone chamber implants (BC) were 4.2 mm in diameter and 6 mm long to allow us to see bone ingrowth into the chamber (BD) and evaluate the bone-to-implant contact at the implant surface (BIC). (B3–6) Surgical procedure: one test (ufgTi) and one control (cpTi) were inserted on one side of the maxilla (B4) and the mandible (B5). The wound was primarily closed. (B7 and B8) Histologic analysis: the BC implant specimens were rinsed in water, dehydrated in ascending ethanol fractions, infiltrated and embedded in methylmethacrylate. Two parameters were applied to characterize the tissue response at the implant surfaces: (1) bone-to-implant contact (BIC) was determined for the new bone matrix, which consisted of osteoid and new mineralized bone matrix deposited along the implant surface (B7). (2) The area fraction of new mineralized bone (BD, bone density), osteoid, and soft tissue within the area of the well-defined implant chamber (B8).

2.2.3. Laser confocal microscopy (LCM). A confocal microscope was used to analyse the surface topography at the micrometre (overview) scale (μsurf explorer, NanoFocus AG, Oberhausen, Germany). The confocal microscope was equipped with a 20× lens focused on a measurement area of 798 × 798 μm^2, with a lateral resolution of 1.56 μm (512 × 512 image points) to capture 3D images. The 3D roughness parameters were calculated using the μsoft Analysis XT software (NanoFocus AG, Oberhausen, Germany) by applying a Gaussian filter with a cut-off wavelength of 50 × 50 μm^2. The following parameters were assessed: S_a μm (arithmetical mean height); S_z μm (maximum height); S_{sk} μm (skewness); S_{dr} μm (developed interfacial area ratio); and S_{pd} μm (density of peaks).

2.2.4. Atomic force microscopy (AFM). AFM characterized the surface topography on the nanometre level with a JPK Nanowizard 4 (JPK Instruments AG, Berlin, Germany) that had a direct drive cantilever holder (Cantilever: high-aspect ratio diamond-like whisker EBD-HAR, NanoAndMore GmbH, resonance frequency: 330 kHz, spring constant: 40 N m^{-1}, typ. tip radius: 7 nm). For each measurement, an area of 1 × 1 μm^2 was scanned at 1 Hz per line and recorded at 1024 × 1024 points. The parametric calculation was performed after form and waviness errors were removed with a Gaussian filter

(0.25 μm) using the μSoft Analysis XT software (NanoFocus AG, Oberhausen, Germany).

2.3. Animal preparation and surgical procedure

Twelve mature Goettinger miniature pigs (average age of 32.7 months; average weight of 50 kg) were used in the experiment. The protocol, which used a well-established study design, was approved by the Committee for Animal Research, State of Bern, Switzerland according to the ARRIVE guidelines (Approval no. 67/14).[12,47] Animals were pre-medicated with ketamine (intramuscular [i.m.] 20 mg kg^{-1}), xylazine (i.m. 2 mg kg^{-1}), atropine (intravenous [i.v.] 0.05 mg kg^{-1}), and midazolam (i.v. 0.5 mg kg^{-1}) so that they could be intubated. Isoflurane (1.0–1.5%) was used for inhalation anaesthesia. Fentanyl patches (5–10 mg kg^{-1}) and more local anaesthesia were administered (Ultracaine, articaine 4% with epinephrine 1 : 200 000, Sanofi-Aventis AG, Vernier, Switzerland) to ensure intra- and postoperative analgesia. The animals received antibiotic prophylaxis for 3 days (Duplocillin LA, 12 000 U.I. kg^{-1}; MSD Animal Health GmbH, Lucerne, Switzerland).

The study design required three surgical interventions per animal.[12,47] The first surgical procedure removed the maxillary incisors and mandibulary premolars (P1, P2 and P3) on both sides. The next two surgical interventions inserted a total of 48 RT and 48 BC implants in a split-mouth design, based on a systematic random protocol. The second surgical intervention was performed 3 months after the teeth were extracted. In this procedure, two RT and two BC implants (ufgTi = test and cpTi = control) were inserted into one side of the maxilla and the mandible (Fig. 1A3–A6 and B3–B6). The primary wound was closed to allow submerged healing. The third surgical intervention was performed after the pigs healed for 4 weeks. The procedure was the same as in the previous surgery, but the implants were inserted on the opposite side of the maxilla and mandible. The pigs were sacrificed after 4 weeks, resulting in healing periods of 4 and 8 weeks per animal (Fig. 1).

2.4. Histologic processing and analysis

The BC implant specimens were rinsed in water, dehydrated in ascending ethanol fractions, infiltrated, and embedded in methylmethacrylate. The embedded blocks were serially sliced into 500 μm-thick ground sections using a slow-speed diamond saw with a coolant (Varicut® VC-50, Leco, Munich, Germany). After they were mounted on acrylic glass slides, the sections were ground to a final thickness of 80 μm and superficially stained with a toluidine blue/McNeal and basic fuchsin combination.[48]

The tissue response at the implant surfaces was characterized with two parameters. (1) Bone-to-implant contact (BIC) was determined for the new bone matrix (osteoid and new mineralized bone matrix deposited along the implant surface). The percentage of BIC was determined using a light microscope by counting intersections through an integrated eyepiece with parallel sampling lines at a magnification of ×250, using a square grid[44] (Fig. 1B7). (2) The area fraction of new mineralized bone (BD, bone density), osteoid, and soft tissue in the well-defined implant chamber was determined using the same grid and magnification (Fig. 1B8).

2.5. Biomechanical torque out analysis

Immediately after sacrifice, specimens with RT implants were cut into individual samples (20 × 20 × 20 mm). Mucosal tissue was removed from the samples to expose the head of the integrated implants. The specimens were embedded in dental plaster (Dental Plaster GC Fujirock® EP, GC Europe, Leuven, Belgium) to prepare them for mechanical testing. After the plaster cured, the implant interfaces were connected to the actuator of a servohydraulic testing machine (MTS Mini Bionix 858, MTS Systems Corporation, Eden Prairie, USA) and lowered into a mould connected to the load cell. A low-melting point alloy (Ostalloy 117, Metallum AG Pratteln, Switzerland – melting point 47 °C) was poured into the mould to create a rigid interface with the plaster and ensure axial alignment of the machine and the implant. The removal torque was tested by rotating the implant counter clockwise at 0.5° s^{-1} until the peak moment was clearly reached. Angle and torque data were continuously sampled at 50 Hz. The RT value was defined as the maximum torque measured. Interface stiffness was defined as the slope (N cm per °) of the quasi-linear segment of the torque–rotation curve; this was calculated using linear regression analysis within the range of 15% to 75% of the peak moment (Fig. 1A7 and 8).

2.6. Micro-CT imaging and analysis

The samples were scanned at 55 kV/600 ms per tomographic projection with a micro-CT Skyscan 1172 (Bruker micro-CT, Kontich, Belgium) at an isotropic voxel size of 12.5 μm. The virtual slices (reconstructions) were obtained using the GPU Recon software for a single PC (Bruker micro-CT, Kontich, Belgium). An experienced evaluator chose an appropriate threshold to identify the mineralized bone. The volume of interest (VOI) was a cylinder (outer diameter: 7 mm; inner diameter: 5 mm), as described previously.[49,50] The CT software (version 1.11, Bruker micro-CT, Kontich, Belgium) was used to segment and morphometrically analyse the images (Fig. 6). The following morphometric parameters were calculated over the VOI: bone volume fraction (BV/TV, %); bone surface density (BS/TV, mm^{-1}); structure model index as a method intended for determining the plate- or rod-like geometry of trabecular structures (SMI);[51] trabecular thickness (Tb.Th, mm); trabecular separation (Tb.Sp, mm); and trabecular number (Tb.N, mm^{-1}).[52]

2.7. Statistical analysis

A nonparametric ANOVA for longitudinal data was applied to determine the impact of the test and control materials at 4 and 8 weeks, first with a global test, and then, in case of significance, with a *post-hoc* test.[53] The *post-hoc* analyses were performed using Wilcoxon signed-rank tests for the paired case, and Mann–Whitney–Wilcoxon tests for the non-paired case. Bonferroni–Holm's method was used to correct for multiple testing. TOST tests were applied to determine if the two groups

were equivalent. The magnitude of the region of similarity was 10% of the median of the values from the control group. *P* values less than 0.05 were considered significant: $p < 0.05$(*), $p < 0.001$(**). All statistical analyses were calculated using an open source R software package (R 3.0.2, extension package nparLD, http://www.r-project.org).

3. Results

3.1. Improved metallographic properties of ufgTi compared to cpTi

UfgTi's mechanical performance was enhanced, as shown by its significantly higher ultimate tensile strength: ufgTi reached 1294.2 MPa, while conventionally processed cpTi was only at 866.6 MPa ($p < 0.001$). The yield strength significantly increased, from 686.4 MPa for cpTi to 1089.8 MPa for ufgTi ($p < 0.001$). The superior mechanical properties of ufgTi were also demonstrated by significantly reduced elongation (19.59% for cpTi; 12.71% for ufgTi; $p < 0.001$) and significantly increased reduction area (43.38% for cpTi; 52.39% for ufgTi; $p < 0.001$). Vickers hardness was higher for ufgTi than for cpTi ($p < 0.0001$), but there was no significant difference in the elastic modulus ($p = 0.8960$).

3.2. Surface characterization

LCM results revealed a surface topography at the micrometre level of similar roughness, using equivalence testing (Fig. 2). The only significant equivalence was for S_a: ufgTi had a significantly higher S_a (1.42 μm) than cpTi (1.35 μm; $p = 0.0180$). There was no significant difference in S_z, S_{sk}, S_{dr} or S_{pd} between cpTi (20.20 ± 1.79 μm, 0.10 ± 0.05, 14.83 ± 1.05% and 1779 ± 99[1 mm^{-2}]) and ufgTi (20.68 ± 1.39 μm, 0.06 ± 0.07, 16.5 ± 0.73% and 1553 ± 114[1 mm^{-2}]) (Fig. 2A1–2 and B1–2).

Analysis of the surface topography revealed nanostructures on ufgTi and cpTi surfaces. The topographies of the nanostructures of nano-patterned ufgTi and cpTi surfaces ($p = 1.000$) were not significantly different. There was a trend of larger height deviation (S_a, nm) and lager surface development (S_{dr}, %) for ufgTi surfaces (13.48 ± 2.78 nm and 227 ± 40%) compared to cpTi surfaces (12.25 ± 1.23 nm and 193 ± 45%) ($p = 1.000$) (Fig. 2A3–4 and B3–4).

Both surfaces were super-hydrophilic, presenting a complete wetting with a contact angle of 0°.

3.3. Histologic analysis

The surgical sites healed uneventfully and without complications (Fig. 3). Of the 192 chambers, 10 were excluded because epithelial cells downgrew into the chambers. There was new and old bone on all implant surfaces. UfgTi and cpTi implants had no apparent dissimilarities. After 4 weeks of healing, osteoid and osteoblasts were seen in direct contact on both surfaces, and after 8 weeks of healing there were signs of bone remodelling, especially in the maxillary samples.

The bone density (BD) was similar for ufgTi and cpTi implants ($p = 1.000$), but there was a significant interaction between jaws and the healing period in the overall testing ($p < 0.001$). In the *post-hoc* test, the BD in the maxilla decreased significantly between the 4th and 8th week, while in the mandible the BD significantly increased over time ($p < 0.001$, Fig. 4A–C).

Total bone-to-implant contact (BIC) on ufgTi and cpTi implants remained unchanged irrespective of the implant material, the jaw into which the BC implants were inserted, or the length of the healing period ($p = 1.000$) (Fig. 4D–F).

3.4. Biomechanical torque out analysis

Overall, torque-out values increased significantly from 4 to 8 weeks and there was no significant difference between ufgTi and cpTi ($p = 1.000$). In the *post-hoc* test, torque-out values increased significantly over time in the maxilla and the mandible for both materials (maxilla: cpTi = 145.57 ± 15.55 N cm to 232.82 ± 23.76 N cm; ufgTi = 141.63 ± 47.23 N cm to 227.4 ± 52.4 N cm; $p < 0.001$; mandible: cpTi = 251.82 ± 41.89 N cm to 303.92 ± 101.65 N cm; ufgTi = 222.57 ± 55.46 N cm to 326.02 ± 82.7 N cm; $p < 0.001$) (Fig. 5A–C).

The interface stiffness was similar for cpTi and ufgTi implants, but there was a significant difference between the jaws ($p = 0.0233$). In the maxilla, the stiffness values increased significantly over time for cpTi and ufgTi (maxilla = cpTi = 43.93 ± 13.35 N cm per ° to 58.28 ± 9.71 N cm per °; ufgTi = 41.88 ± 9.61 N cm per ° to 57.03 ± 9.04 N cm per °). In the mandible, these values did not change significantly over time (mandible: cpTi = 59.9 ± 9.2 N cm per ° to 61.7 ± 13.15 N cm per °; ufgTi = 61.13 ± 11.02 N cm per ° to 62.63 ± 5.05 N cm per °) (Fig. 5D and E).

3.5. Micro-CT imaging and analysis

Micro-CT analysis of the peri-implant bone volume determined the effect of these biomaterials on the bony architecture of the mandible and the maxilla (Table 1 and Fig. 6). The bone mineral density (BMD, g cm^{-3}) was significantly higher in the mandible than in the maxilla at 4 weeks ($p = 0.0011$) and at 8 weeks ($p = 0.0037$) and did not increase over time. The bone volume fraction (BV/TV, %) was similar in both jaws. The structure model index (SMI) revealed significantly different structures of the maxilla and the mandible ($p \leq 0.0001$) (Fig. 6). The trabecular number was not significantly different between the jaws ($p = 0.1956$), but the trabeculae were thicker in the maxilla at both time points (4 weeks, $p = 0.0071$; 8 weeks, $p = 0.013$).

4. Discussion

The metallographic properties of ultrafine-grained titanium (ufgTi) implants with a hydrophilic nano-patterned surface were superior to those of cpTi implants, except for the elastic modulus. It would thus be very interesting to try using ufgTi as an implant material in small-diameter implants designed to reduce the invasiveness of surgical procedures. Although ufgTi had superior mechanical properties, its surface topography in the nanometre range was similar to that of cpTi. Our histomor-

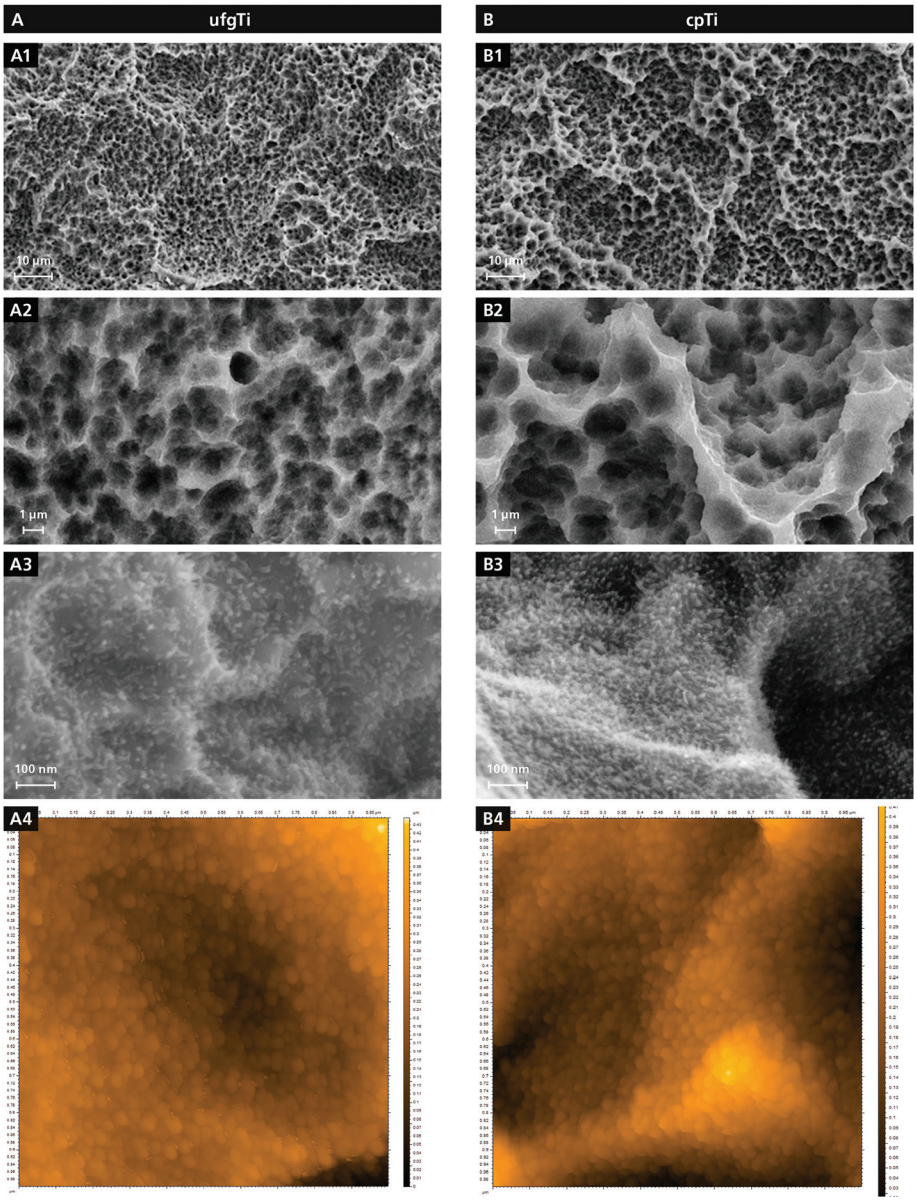

Fig. 2 Surface characterization. (A) Test: ufgTi surface analysed using field-emission-gun scanning electron microscopy (SEM), laser confocal microscopy (LCM, surface topography at the micrometre level) and atomic force microscopy (AFM, surface topography at the nanometre level). (A1) The 10 μm level. (A2) The 1 μm level. (A3) The 100 nm level. (A4) Atomic force microscopy at the nanometre level. (B) Control: cpTi surface analysed by field-emission-gun scanning electron microscopy (SEM), laser confocal microscopy (LCM, surface topography at the micrometre level) and atomic force microscopy (AFM, surface topography at the nanometre level). (B1) The 10 μm level. (B2) The 1 μm level. (B3) The 100 nm level. (B4) Atomic force microscopy at the nanometre level.

phometric and biomechanical analyses found that ufgTi did not have a negative effect in *in vivo* testing in the maxilla and the mandible of miniature pigs, and found no significant differences between ufgTi and cpTi. The bony microarchitecture of the maxilla and the mandible had a significant effect on biomechanical torque out values and bone density during healing. During healing, the bone density decreased in the maxilla, but increased in the mandible ($p < 0.001$); so the torque out values were significantly lower for the maxilla than those for the mandible. Irrespective of the bony microarchitecture, ufgTi and cpTi implants with a hydrophilic nano-patterned surface achieved high bone-to-implant contact (BIC) values even when the bone mineral density was low.

The surface morphology of ufgTi appears to be more densely spaced, with more peaks on the nanoscale. Some speculate that these peaks may help to improve cell attachment and to spread stem cells,[26] but the underlying mechanism is not yet understood. We found only small differences in the surface characteristics of ufgTi with a higher S_a value of 1.42 μm at the micrometre level, whereas at the nanometre

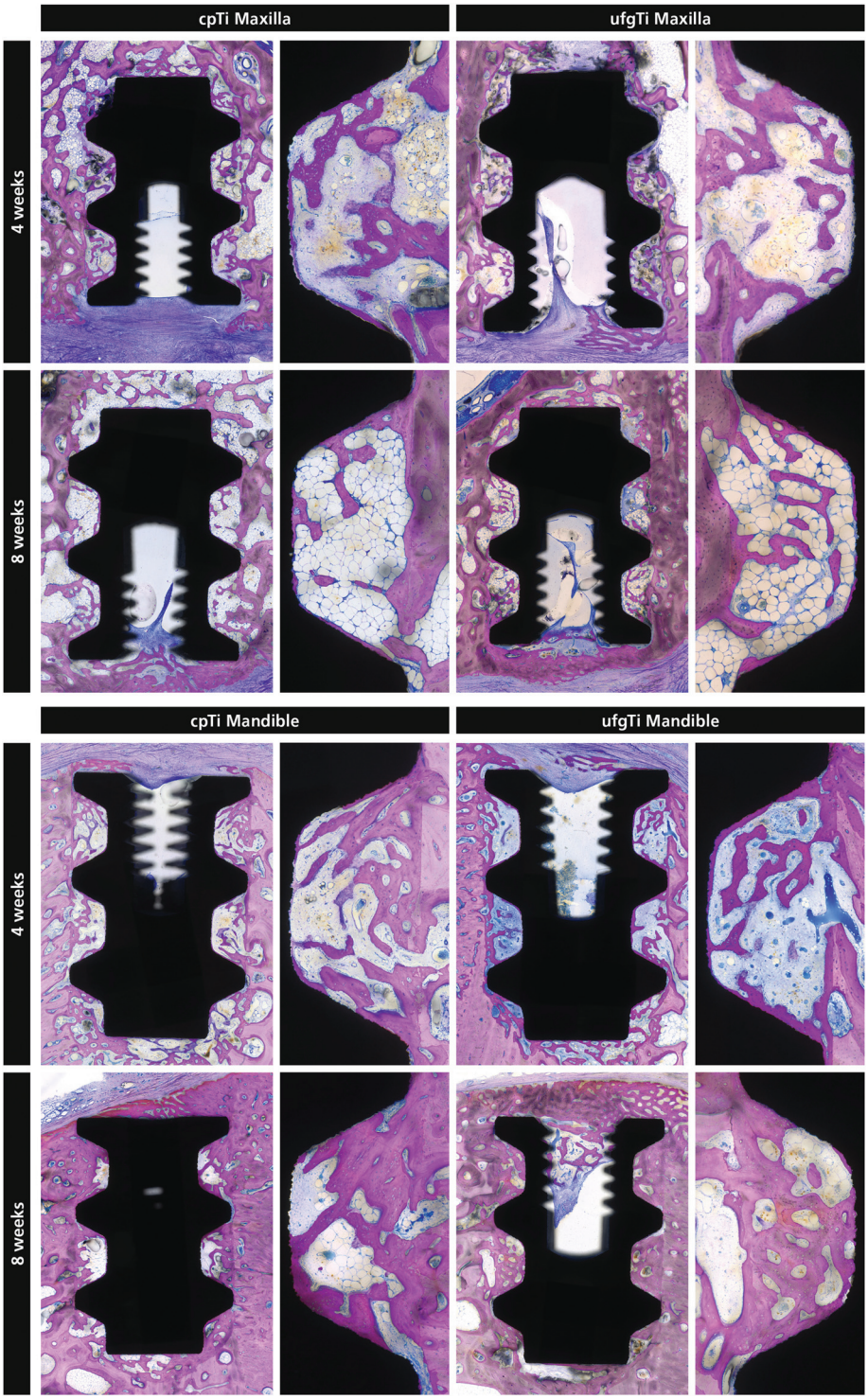

Fig. 3 Histology. The surgical sites healed uneventfully in all animals, without complications. New and old bones were found on all implant surfaces. There were no apparent dissimilarities between ufgTi and cpTi implants. After 4 weeks of healing, osteoid and osteoblasts were in direct contact with the surfaces; after 8 weeks of healing, there were signs of bone remodelling, especially in the maxillary samples.

level no significant differences were observed. The richness of the surface morphology of ufgTi has been described as an important factor in controlling the enhanced attachment and spreading of stem cells and promoting cell adhesion.[26,27] Studies have shown the cell compatibility of ufgTi,[26,54,55] but few have analysed the *in vivo* performance. Estrin *et al.* found no difference in BIC values when they inserted cpTi and ufgTi with a rather smooth surface into the rabbit tibia.[56] A recent *in*

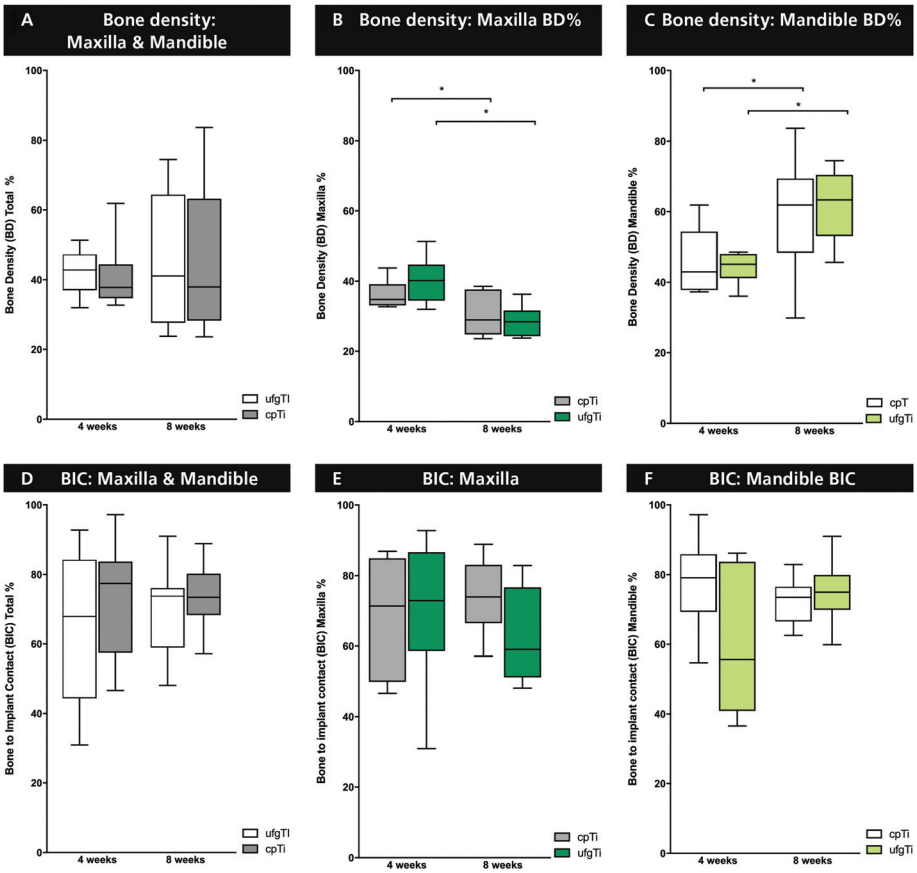

Fig. 4 Histomorphometric analysis. (A–C) Bone density (BD): BD revealed no significant differences between ufgTi and cpTi implants (p = 1.000), but there was significant interaction between jaws and the healing period, overall (p < 0.001). In the *post-hoc* test, BD in the maxilla decreased significantly from 4 to 8 weeks, whereas in the mandible the BD significantly increased over time (p < 0.001). (D–F) Bone to implant contact (BIC): BIC remained unchanged irrespective of the implant material, the jaw in which the BC implants were inserted, or the length of the healing period (p = 1.000).

vivo experiment investigated surface characteristics of sand-blasted and acid-etched ufgTi after implanting it into the lateral condyle of the femur of New Zealand rabbits,[57] and reported surface characteristics slightly different from those we identified. This study used test and control implants with higher S_a-values than we did and the surface wettability values in their study were 65 for ufgTi and 106 for cpTi; so ufgTi was more hydrophilic in their study. After 3 months of healing, ufgTi had significantly higher pullout forces (506 N) than cpTi (417 N), which may be influenced by the increased hydrophilicity of ufgTi. Although the ufgTi bulk material is of higher strength and toughness, the surface properties are very similar to cpTi and showed no negative effect on osseointegration.

The bone microarchitecture of the maxilla and the mandible had significant implications on the biomechanical torque out values and bone density during healing. The significant influence of the jaw's bone microarchitecture on the removal torque is poorly understood and we found no literature reports to show that it had been investigated. Since maxillary implants have higher failure rates, especially in short implant designs, our findings have clinical implications.[58] This increased failure rate in maxillary implants is related to the maxillary microarchitecture and to the healing capacity, possibly caused by biomechanical limitations. Interestingly, the microarchitecture of the jaws did not influence the BIC values. We saw high BIC values in environments where the bone mineral density was lower (BMDg cm^{-3}); so the amount of new bone apposition does not correlate with the bone density in the chamber. But the microarchitecture of the jaw and the amount of newly formed bone in the chambers may help reduce resistance to the removal torque. Studies have shown that the insertion torque significantly depends on the bone microarchitecture, particularly for SMI, BV/TV and BMD.[50] A recent study showed that BV/TV and trabecular orientation essentially control the mechanical properties of trabecular bone.[59] Therefore, the bone microarchitecture significantly influences osseointegration and needs to be considered when assessing experimental *in vivo* studies.

Our results highlight the effectiveness of hydrophilic nano-patterned surfaces in osseointegration. Even in a low-bone-density environment of the maxilla, where the peri-implant bone structure did not consolidate after 8 weeks, the torque out parameters increased significantly, and therefore osseointegration remained high. Our histomorphometric findings are

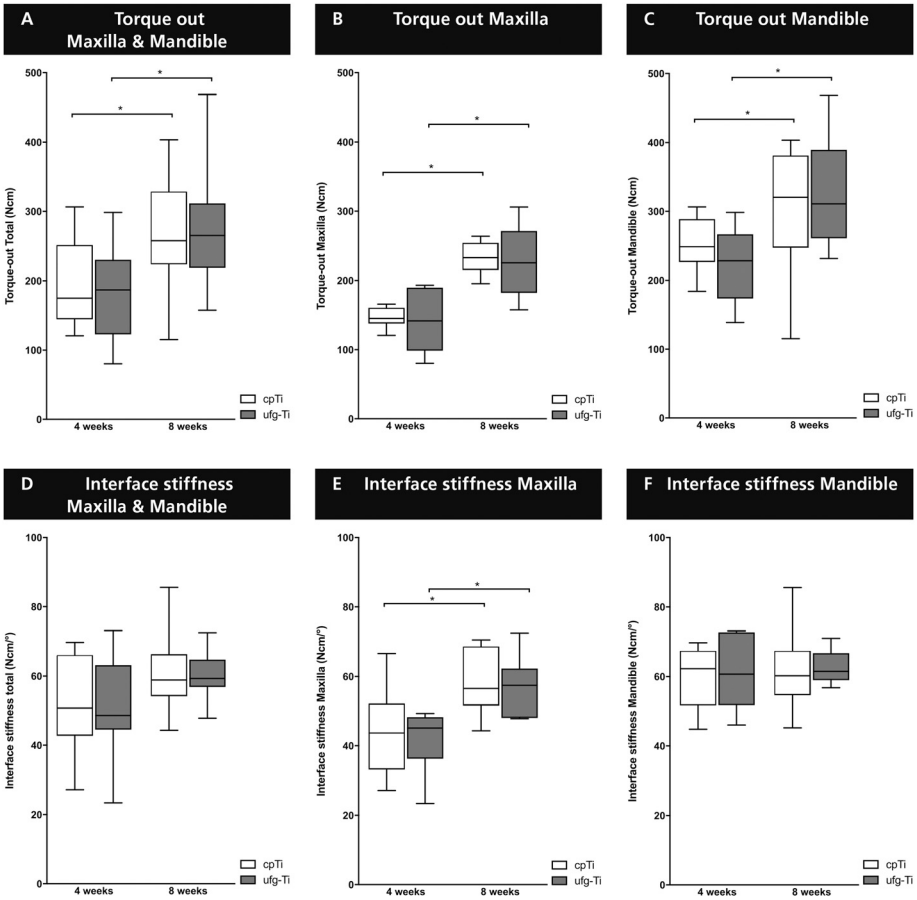

Fig. 5 Biomechanical analysis and interface stiffness. (A–C) Torque-out analysis: overall, torque-out values increased significantly from 4 to 8 weeks and there was no significant difference between ufgTi and cpTi (p = 1.000). In the *post-hoc* test, torque-out values increased significantly over time in the maxilla and the mandible for both materials (maxilla: cpTi = 145.57 ± 15.55 N cm to 232.82 ± 23.76 N cm; ufgTi = 141.63 ± 47.23 N cm to 227.4 ± 52.4 N cm; $p < 0.001$; mandible: cpTi = 251.82 ± 41.89 N cm to 303.92 ± 101.65 N cm; ufgTi = 222.57 ± 55.46 N cm to 326.02 ± 82.7 N cm; $p < 0.001$). (D–F) Interface stiffness: interface stiffness was similar for cpTi and ufgTi implants, but there was a significant difference between the jaws (p = 0.0233). In the maxilla, the stiffness values increased significantly over time for cpTi and ufgTi (maxilla = cpTi = 43.93 ± 13.35 N cm per ° to 58.28 ± 9.71 N cm per °; ufgTi = 41.88 ± 9.61 N cm per ° to 57.03 ± 9.04 N cm per °). In the mandible, these values did not change significantly over time (mandible: cpTi = 59.9 ± 9.2 N cm per ° to 61.7 ± 13.15 N cm per °; ufgTi = 61.13 ± 11.02 N cm per ° to 62.63 ± 5.05 N cm per °).

Table 1 Microarchitecture of the peri-implant bone

	Maxilla		Mandible	
	4 weeks	8 weeks	4 weeks	8 weeks
Bone mineral density (BMD) (g cm^{-3})	0.64 ± 0.04	0.71 ± 0.05	1.00 ± 0.02	0.97 ± 0.11
Bone volume fraction BV/TV (%)	31.41 ± 3.79	41.48 ± 13.78	44.06 ± 3.63	49.11 ± 1.56
Structure model index (SMI)	−2.57 ± 1.09	−3.85 ± 2.61	−8.97 ± 2.05	−12.28 ± 0.81
Bone surface density BS/TV (1 mm^{-1})	4.69 ± 0.26	5.81 ± 2.15	10.08 ± 4.27	8.31 ± 1.94
Trabecular thickness Tb.Th (μm)	206.5 ± 15.87	211.30 ± 22.36	109.66 ± 28.18	129.41 ± 34.61
Trabecular number Tb.N (1 mm^{-1})	1.51 ± 0.13	2.02 ± 0.85	4.29 ± 1.61	3.55 ± 1.77

consistent with those of recent publications examining microrough hydrophilic surfaces on different titanium alloys. These studies, in a similar experimental setting, found BD values between 29% and 62% and BIC values between 70% and 84% for new bone apposition onto cpTi and TiZr alloy after 4 and 8 weeks of healing, and found that the Ti6Al4V alloy had significantly inferior BIC values (27%–29%).[44,45] Gottlow *et al.* examined the removal torque values and interfacial stiffness of hydrophilic TiZr alloy implants with an SLA surface at mandibular sites with a healing period of 4 weeks.[45] They found a similar range of torque out values (cpTi: 204.7 N cm, TiZr alloy: 230.9 N cm), but substantially lower interfacial stiffness (cpTi: 41.7 N cm per °, TiZr alloy: 48.5 N cm per °). In our study, osseointegration had progressed significantly in maxil-

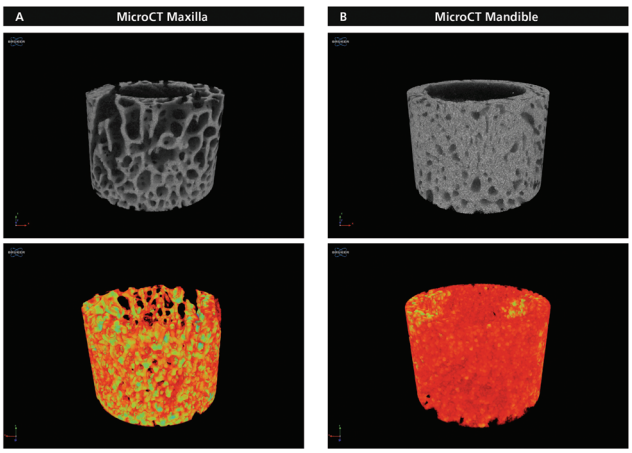

Fig. 6 Micro-CT analysis. To better understand the effect of the biomaterials on the bone architecture, we conducted a micro-CT analysis of the peri-implant bone volume in the mandible (B) and the maxilla (A). Bone mineral density (BMD, g cm^{-3}) was significantly higher in the mandible than in the maxilla at both 4 weeks (p = 0.0011) and 8 weeks (p = 0.0037); it did not increase over time. The bone volume fraction (BV/TV, %) was similar for both jaws. The structure model index (SMI) showed significantly different structures in the maxilla and mandible ($p \leq 0.0001$). The trabecular number was similar for both jaws (p = 0.1956), but the trabecular thickness revealed thicker trabeculae for the maxilla at both 4 weeks (p = 0.0071) and 8 weeks (p = 0.013).

lary and mandibular sites: the RT values at 8 weeks were significantly higher than those at 4 weeks. This progression of osseointegration could be related to the consolidation of new bone formation.[60,61] This hypothesis was valid for the mandible, but not for the maxilla. In the maxilla the RT values increased over time and high BIC values were obtained, although the bone became less dense as it healed. In the present investigation osseointegration at hydrophilic nano-patterned surfaces remained high irrespective of the bone microarchitecture and even when the bone mineral density was low.

Our study has several limitations. Our results cannot be clinically applied because miniature pigs regenerate bone faster than human beings. We also examined dental implants under non-loaded conditions; under functional loading, the results may differ. We used special bone chamber (BC) implants designed for animal experiments; so our findings cannot be extrapolated to clinical use. The implants were stabilized by press-fit into the osteotomy site to create a secluded and well-defined space that allowed us to carefully standardize the delineation process in the early phases of bone formation.[12,44,45,62] In these custom-made implants, the distance between the biomaterial surface and the pristine bone is greater than it would be for conventional screw-type dental implants typically used in clinical situations.

5. Conclusions

Ultrafine-grained titanium (ufgTi) reinforced by grain refinement showed superior metallographic properties compared to cpTi. It formed a hydrophilic nano-patterned surface with high levels of osseointegration even when the bone mineral density was low. These observations suggest that the use of ufgTi has great potential as a future strategy for the development of small diameter implants to enable less invasive treatment concepts, reduce patient morbidity, and may also lower the costs of patient care.

Conflicts of interest

The authors received no financial support and declare no potential conflicts of interest with respect to the authorship and/or publication of this article.

Acknowledgements

We thank Prof A. Wennerberg for revising the manuscript and her valuable contribution and acknowledge Gabriel Fischer, Institute of Mathematical Statistics and Actuarial Science, University of Bern, for performing the statistical analysis. We thank Kali Tal for her editorial suggestions. The study was supported by a grant from Straumann AG, Basel, Switzerland.

References

1 D. Buser, L. Sennerby and H. De Bruyn, *Periodontol. 2000*, 2017, **73**, 7–21.
2 P. I. Branemark, R. Adell, U. Breine, B. O. Hansson, J. Lindstrom and A. Ohlsson, *Scand. J. Plast. Reconstr. Surg.*, 1969, **3**, 81–100.
3 P. I. Branemark, B. O. Hansson, R. Adell, U. Breine, J. Lindstrom, O. Hallen and A. Ohman, *Scand. J. Plast Reconstr. Surg. Suppl.*, 1977, **16**, 1–132.
4 A. Schroeder, O. Pohler and F. Sutter, *SSO Schweiz. Monatsschr. Zahnheilkd.*, 1976, **86**, 713–727.
5 A. Schroeder, E. van der Zypen, H. Stich and F. Sutter, *J. Maxillofac. Surg.*, 1981, **9**, 15–25.
6 R. Adell, U. Lekholm, B. Rockler and P. I. Branemark, *Int. J. Oral Surg.*, 1981, **10**, 387–416.
7 C. A. Babbush, J. N. Kent and D. J. Misiek, *J. Oral Maxillofac. Surg.*, 1986, **44**, 274–282.
8 D. Buser, R. Mericske-Stern, J. P. Bernard, A. Behneke, N. Behneke, H. P. Hirt, U. C. Belser and N. P. Lang, *Clin. Oral. Implants Res.*, 1997, **8**, 161–172.
9 U. Lekholm, K. Grondahl and T. Jemt, *Clin. Implant Dent. Relat. Res.*, 2006, **8**, 178–186.
10 V. Chappuis, R. Buser, U. Bragger, M. M. Bornstein, G. E. Salvi and D. Buser, *Clin. Implant Dent. Relat. Res.*, 2013, **15**, 780–790.
11 B. D. Boyan, T. W. Hummert, D. D. Dean and Z. Schwartz, *Biomaterials*, 1996, **17**, 137–146.
12 D. Buser, N. Broggini, M. Wieland, R. K. Schenk, A. J. Denzer, D. L. Cochran, B. Hoffmann, A. Lussi and S. G. Steinemann, *J. Dent. Res.*, 2004, **83**, 529–533.

13 F. Rupp, L. Scheideler, N. Olshanska, M. de Wild, M. Wieland and J. Geis-Gerstorfer, *J. Biomed. Mater. Res., Part A*, 2006, **76**, 323–334.
14 X. Liu, J. Y. Lim, H. J. Donahue, R. Dhurjati, A. M. Mastro and E. A. Vogler, *Biomaterials*, 2007, **28**, 4535–4550.
15 Collaborators, *Lancet*, 2017, **390**, 1211–1259.
16 H. J. Rack and J. I. Qazi, *Mater. Sci. Eng., C*, 2006, **26**, 1269–1277.
17 N. J. Hallab, S. Anderson, M. Caicedo, A. Brasher, K. Mikecz and J. J. Jacobs, *J. Biomed. Mater. Res., Part A*, 2005, **74**, 124–140.
18 G. M. Keegan, I. D. Learmonth and C. P. Case, *J. Bone Joint Surg. Br.*, 2007, **89**, 567–573.
19 A. Y. Vinogradov, V. V. Stolyarov, S. Hashimoto and R. Z. Valiev, *Mater. Sci. Eng., A*, 2001, **318**, 163–173.
20 R. Z. L. Valiev and T. G. Langdon, *Prog. Mater. Sci.*, 2006, **7**, 881–981.
21 Y. Estrin and A. Vinogradov, *Acta Mater.*, 2013, **61**, 782–817.
22 K. Nakashima, Z. Horita, M. Nemoto and T. Langdon, *Acta Mater.*, 1998, **46**, 1589–1599.
23 Y. J. Chen, Y. J. Li, J. C. Walmsley, S. Dumoulin, S. S. Gireesh, S. Armada, P. C. Skaret and H. J. Roven, *Scr. Mater.*, 2011, **64**, 904–907.
24 I. P. Semenova, R. Z. Valiev, E. B. Yakushina, G. H. Salimgareeva and T. C. Lowe, *J. Mater. Sci.*, 2008, **43**, 7354–7359.
25 C. Yao, E. B. Slamovich, J. I. Qazi, H. J. Rack and T. J. Webster, *Ceram. Trans.*, 2005, **159**, 239–245.
26 Y. Estrin, E. P. Ivanova, A. Michalska, V. K. Truong, R. Lapovok and R. Boyd, *Acta Biomater.*, 2011, **7**, 900–906.
27 V. K. Truong, R. Lapovok, Y. S. Estrin, S. Rundell, J. Y. Wang, C. J. Fluke, R. J. Crawford and E. P. Ivanova, *Biomaterials*, 2010, **31**, 3674–3683.
28 S. Franz, S. Rammelt, D. Scharnweber and J. C. Simon, *Biomaterials*, 2011, **32**, 6692–6709.
29 C. M. Bhadra, V. K. Truong, V. T. Pham, M. Al Kobaisi, G. Seniutinas, J. Y. Wang, S. Juodkazis, R. J. Crawford and E. P. Ivanova, *Sci. Rep.*, 2015, **5**, 16817.
30 D. L. Cochran, R. K. Schenk, A. Lussi, F. L. Higginbottom and D. Buser, *J. Biomed. Mater. Res.*, 1998, **40**, 1–11.
31 F. Schwarz, M. Wieland, Z. Schwartz, G. Zhao, F. Rupp, J. Geis-Gerstorfer, A. Schedle, N. Broggini, M. M. Bornstein, D. Buser, S. J. Ferguson, J. Becker, B. D. Boyan and D. L. Cochran, *J. Biomed. Mater. Res., Part B*, 2009, **88**, 544–557.
32 A. Wennerberg and T. Albrektsson, *Clin. Oral. Implants Res.*, 2009, **20**(Suppl 4), 172–184.
33 V. Chappuis, L. Rahman, R. Buser, S. F. M. Janner, U. C. Belser and D. Buser, *J. Dent. Res.*, 2018, **97**, 266–274.
34 G. Mendonca, D. B. Mendonca, F. J. Aragao and L. F. Cooper, *Biomaterials*, 2008, **29**, 3822–3835.
35 G. Balasundaram, M. Sato and T. J. Webster, *Biomaterials*, 2006, **27**, 2798–2805.
36 E. A. Cavalcanti-Adam, T. Volberg, A. Micoulet, H. Kessler, B. Geiger and J. P. Spatz, *Biophys. J.*, 2007, **92**, 2964–2974.
37 S. N. Rodrigues, I. C. Goncalves, M. C. Martins, M. A. Barbosa and B. D. Ratner, *Biomaterials*, 2006, **27**, 5357–5367.
38 Y. Arima and H. Iwata, *Biomaterials*, 2007, **28**, 3074–3082.
39 T. J. Webster, C. Ergun, R. H. Doremus, R. W. Siegel and R. Bizios, *J. Biomed. Mater. Res.*, 2000, **51**, 475–483.
40 L. Le Guehennec, A. Soueidan, P. Layrolle and Y. Amouriq, *Dent. Mater.*, 2007, **23**, 844–854.
41 M. P. Monopoli, C. Aberg, A. Salvati and K. A. Dawson, *Nat. Nanotechnol.*, 2012, **7**, 779–786.
42 R. Z. Valiev, I. P. Semenova, E. B. Yakushina and G. K. Salimgareeva, *Nanostructured commercially pure titanium for biomedicine and a method for producing a rod therefrom* (http://patft.uspto.gov), 2014.
43 S. J. Ferguson, N. Broggini, M. Wieland, M. de Wild, F. Rupp, J. Geis-Gerstorfer, D. L. Cochran and D. Buser, *J. Biomed. Mater. Res., Part A*, 2006, **78**, 291–297.
44 N. Saulacic, D. D. Bosshardt, M. M. Bornstein, S. Berner and D. Buser, *Eur. Cells Mater.*, 2012, **23**, 273–286; discussion 286-278.
45 J. Gottlow, M. Dard, F. Kjellson, M. Obrecht and L. Sennerby, *Clin. Implant Dent. Relat. Res.*, 2012, **14**, 538–545.
46 B. S. Kopf, S. Ruch, S. Berner, N. D. Spencer and K. Maniura-Weber, *J. Biomed. Mater. Res., Part A*, 2015, **103**, 2661–2672.
47 V. Chappuis, Y. Cavusoglu, R. Gruber, U. Kuchler, D. Buser and D. D. Bosshardt, *Clin. Implant Dent. Relat. Res.*, 2015, **18**, 686–698.
48 R. K. Schenk, A. J. Olah and W. Herrmann, *Preparation of calcified tissues for light microscopy*, Elsevier, Amsterdam, 1984.
49 M. L. Bouxsein, S. K. Boyd, B. A. Christiansen, R. E. Guldberg, K. J. Jepsen and R. Muller, *J. Bone Miner. Res.*, 2010, **25**, 1468–1486.
50 R. Ab-Lazid, E. Perilli, M. K. Ryan, J. J. Costi and K. J. Reynolds, *J. Biomech.*, 2014, **47**, 347–353.
51 T. Hildebrand and P. Ruegsegger, *Comput. Methods Biomech. Biomed. Engin.*, 1997, **1**, 15–23.
52 E. Perilli, I. H. Parkinson and K. J. Reynolds, *Ann. Ist. Super. Sanita*, 2012, **48**, 75–82.
53 E. Brunner, S. Domhof and F. Langer, *Nonparametric analysis of longitudinal data in factorial experiments*, J. Wiley & Sons, New York, 2002.
54 J. W. Park, Y. J. Kim, C. H. Park, D. H. Lee, Y. G. Ko, J. H. Jang and C. S. Lee, *Acta Biomater.*, 2009, **5**, 3272–3280.
55 C. Y. Zheng, F. L. Nie, Y. F. Zheng, Y. Cheng, S. C. Wei and R. Z. Valiev, *Appl. Surf. Sci.*, 2011, **257**, 5634–5640.
56 Y. Estrin, H. E. Kim, R. Lapovok, H. P. Ng and J. H. Jo, *BioMed Res. Int.*, 2013, DOI: 10.1155/2013/914764.
57 B. An, Z. Li, X. Diao, H. Xin, Q. Zhang, X. Jia, Y. Wu, K. Li and Y. Guo, *Mater. Sci. Eng., C*, 2016, **67**, 34–41.
58 M. Srinivasan, L. Vazquez, P. Rieder, O. Moraguez, J. P. Bernard and U. C. Belser, *Clin. Oral. Implants Res.*, 2014, **25**, 539–545.

59 S. N. Musy, G. Maquer, J. Panyasantisuk, J. Wandel and P. K. Zysset, *J. Mech. Behav. Biomed. Mater.*, 2017, **65**, 808–813.
60 R. Jimbo, Y. Naito, S. Galli, S. Berner, M. Dard and A. Wennerberg, *Clin. Implant Dent. Relat. Res.*, 2015, **17**(Suppl 2), e670–e678.
61 S. Galli, R. Jimbo, Y. Naito, S. Berner, M. Dard and A. Wennerberg, *Clin. Oral. Implants Res.*, 2017, **28**, 1234–1240.
62 T. Berglundh, I. Abrahamsson, N. P. Lang and J. Lindhe, *Clin. Oral. Implants Res.*, 2003, **14**, 251–262.